Outer midplane scrape-off layer profiles and turbulence in simulations of Alcator C-Mod inner-wall limited discharges

Federico D. Halpern, Brian LaBombard, James L. Terry, and Stewart J. Zweben

---

Articles you may be interested in

A refined understanding of compressibility effects on the stability of drift ballooning modes
Physics of Plasmas **24**, 072504 (2017); 10.1063/1.4990430

Global 3D two-fluid simulations of the tokamak edge region: Turbulence, transport, profile evolution, and spontaneous E × B rotation
Physics of Plasmas **24**, 055903 (2017); 10.1063/1.4978885

Linear interaction and relative role of the ion temperature gradient and trapped electron modes in the reactor-relevant finite beta plasma condition
Physics of Plasmas **24**, 072501 (2017); 10.1063/1.4990071

Two-fluid tearing mode instability in cylindrical geometry
Physics of Plasmas **24**, 072102 (2017); 10.1063/1.4986116

Radial acceleration of geodesic acoustic modes in the presence of a temperature gradient
Physics of Plasmas **24**, 072503 (2017); 10.1063/1.4990074

Alfvén eigenmode stability and critical gradient energetic particle transport using the Trapped-Gyro-Landau-Fluid model
Physics of Plasmas **24**, 072305 (2017); 10.1063/1.4989716

Outer midplane scrape-off layer profiles and turbulence in simulations of Alcator C-Mod inner-wall limited discharges

Federico D. Halpern,[1,2,a)] Brian LaBombard,[3] James L. Terry,[3] and Stewart J. Zweben[4]
[1]*General Atomics, P.O. Box 85608, San Diego, California 92186-5608, USA*
[2]*École Polytechnique Fédérale de Lausanne (EPFL), Swiss Plasma Center, CH-1015 Lausanne, Switzerland*
[3]*Massachusetts Institute of Technology, 77 Massachusetts Avenue, Cambridge, Massachusetts 02139, USA*
[4]*Princeton Plasma Physics Laboratory, Princeton, New Jersey 08540, USA*

A region of steep plasma gradients, the so-called "narrow-feature," has been found in the near scrape-off layer (SOL) of inner-wall limited (IWL) discharges. Dedicated IWL discharges were carried out in Alcator C-Mod [Marmar *et al.*, Nucl. Fusion 55, 104020 (2015)] to study this phenomenon, allowing detailed observations of the plasma profiles and fluctuations. Langmuir probe (LP) measurements show a clear two-decay length n_e and T_e profile structure at the outer midplane. The Gas-Puff Imaging (GPI) diagnostic shows large turbulent fluctuations across the last closed flux-surface, hence supporting the hypothesis that turbulent phenomena play a role in setting the profile steepness. Flux-driven non-linear turbulence simulations of two C-Mod discharges have been carried out, allowing a three-way comparison between LP, GPI, and simulation data. Observations and simulations correlate the steep gradient region characterizing the narrow feature with sheared poloidal flows and a deviation of the plasma potential from its floating value. The $\mathbf{E} \times \mathbf{B}$ shear rate exceeds the linear ballooning growth rate, indicating that the narrow feature could result from the effects of sheared flows, although causality could not be established. The fluctuation level in the narrow feature remains of order unity across the entire SOL, indicating that the transport reduction in the near-SOL cannot result from a simple quench rule. *Published by AIP Publishing.* [http://dx.doi.org/10.1063/1.4989705]

I. INTRODUCTION

An extensive study of L-mode inner-wall limiter (IWL) discharges in Alcator C-Mod, DIII-D, COMPASS, JET, TCV, and other tokamaks has determined that the scrape-off layer (SOL) plasma profiles have a two decay-length structure.[1] Just outside the last-closed flux surface (LCFS), the parallel heat-flux ($q_\parallel \sim nc_sT$) drops very rapidly, with a decay length $\lambda_q \approx -q_\parallel/\nabla q_\parallel$ of a few mm, while the main-SOL heat-flux decay length can be of a few centimeters.[2] (The narrow feature heat-flux decay length is here denominated λ_q, while $\lambda_{q,main}$ will refer to the far-SOL. An equivalent notation is adopted for the characteristic density, temperature, or pressure gradient lengths.) The same decay length structure can be inferred for the density and temperature profiles when using Langmuir probes (LPs). The steep gradient region is referred to as a "narrow heat-flux feature" in the literature.[3–6] Based on the multi-machine study, the ITER narrow-feature λ_q is projected to be about 4 mm for the IWL scenario, which prompted a redesign of the inner-wall panels.

The objective of this paper is to shed light on the physical mechanisms giving rise to the narrow feature, through a combination of turbulence simulations and state-of-the-art plasma diagnostics. We describe and analyze two Alcator C-Mod L-mode IWL discharges with $B_T = 4.0$, with a magnetic safety factor $q_a = 2.75$ and 4.25 at the LCFS, and with an elongation $\kappa \approx 1.2$. The C-Mod plasma profiles have been

measured with reciprocating Langmuir probes (RCP) at the outer midplane (OMP), showing a significant profile steepness just outside the LCFS. Previously published data show that the profiles are similarly steep at other probe insertion points (e.g., high-field side or vertical probes (VPs), see Ref. 7). We also describe OMP Gas-Puff Imaging (GPI) measurements that allow a characterization of turbulent phenomena within the near-SOL. These two discharges provide an ideal scenario for a comparison against non-linear, 3D flux-driven turbulence simulations carried out with the GBS code, a fully verified and validated implementation of the fluid drift-Braginskii equations.[8,9] The simulation setup and numerical details are similar to that used in our previous work.[10] We emphasize that, rather than attempting to extrapolate the variation of the profile steepness with the plasma parameters (e.g., the I_p^{-1} scaling reported by several authors), our objective is to compare high-resolution diagnostics and non-linear simulations to help understand the cross-field transport dynamics.

While the ITER inner-wall design is now fixed, the physical mechanisms regulating the narrow-feature decay length are still not well understood. Kocan's multi-machine study[1] found that λ_q is, roughly, inversely proportional to the poloidal magnetic field. Hence, λ_q follows a scaling similar to those found for H-mode diverted discharges.[11–13] In combination with previous results for diverted H-modes, EDA H-modes, and Ohmic L-mode plasmas in C-Mod and DIII-D,[14–16] this points towards the possibility that similar physics could control cross-field SOL transport across a

a)Electronic mail: halpernf@fusion.gat.com

wide range of discharge scenarios and plasma parameters. Thus, besides our stated objective of characterizing the narrow feature, the analysis presented herein may be relevant to analyze and clarify the SOL transport physics beyond the IWL configuration.

Direct comparisons between SOL turbulence measurements and edge turbulence simulations have been carried out initially using 2D codes such as ESEL[17] and SOLT.[18] These seemingly simple models (e.g., ideal interchange filament dynamics) in fact recover many quantitative measurements such as filament structure, propagation, and transport intermittency.[19–22] The disadvantage of 2D models is that the effects of parallel flows, sheaths, and drift modes must be introduced through analytical closures. Recent advances in computer hardware have enabled 3D simulations of the plasma edge, such as those carried out with the GEMR δf gyrofluid code.[23,24] GEMR simulations of generic IWL plasmas including drift physics are, to our knowledge, the first to show a narrow layer of steepened profiles near the LCFS.[24] In GEMR simulations of C-Mod,[23] the input parameters were taken from Langmuir probe measurements, and the turbulent fluctuations were reproduced rather than the profiles. More recently, full-moment, flux-driven simulations of the C-Mod SOL were carried out with the GBS drift-Braginskii code,[10] showing good agreement with GPI data while reproducing the observed profiles. The blob filament dynamics in MAST has been modeled using the BOUT++ framework.[25,26] More recent work demonstrates total-f electrostatic gyrokinetic simulations of the SOL turbulent dynamics including neoclassical effects.[27]

In our previous publication,[10] we compared the fluctuation moments and correlation lengths averaged across the far SOL using the 2007 IWL C-Mod discharges. Data from the 2014 campaign used in the present paper have significantly improved diagnostics, which allow us to investigate the plasma profiles and the variation of the turbulent characteristics with the SOL radius. Certainly, the discovery of the steep gradient region, with the addition of reliable measurements of the plasma profile gradients, offers a compelling reason to revise the IWL plasma scenarios and carry out a more detailed comparison.

The three way comparison between RCP, GPI measurements, and GBS simulations show a good three-way match. The flux-driven GBS simulations result in a two decay-length profile, although the code fails to reproduce the narrow feature strength found in the RCP profiles. (By strength we mean the relative weight of the short exponential decay profile with respect to the far-SOL.) In the turbulence simulations, the time averaged gradient lengths result entirely from a balance between turbulent eddies (which have roughly the GPI measured mode structure) and sheath losses. Neoclassical orbit effects are not included in the GBS simulations. Electric potential RCP measurements reveal, and GBS simulations reproduce, a strong flow-shear layer within the narrow feature. Despite the large shearing rate, which is of the order of the turbulent growth rate, we find within the narrow feature a relative fluctuation level $\delta n / \langle n \rangle \approx 15\%$ in the mirror Langmuir probe (MLP) and GPI measurements as well as in the non-linear simulations. Altogether, experimental evidence and the GBS simulations indicate that turbulent phenomena play a role in setting the near-SOL profile steepness in C-Mod.

The paper is organized as follows. Section II describes the plasma conditions and diagnostics used for the C-Mod experiments, while Sec. III describes the GBS simulations of the C-Mod SOL. These two sections contain technical details on the observations, the simulation setup, and the data analysis carried out. Section IV contrasts the results of the numerical simulations with the experimental observation. Finally, Sec. V gives a summary and a discussion of the findings of this work.

II. PLASMA SCENARIOS AND EXPERIMENTAL SETUP

Alcator C-Mod is a high-field ($B_T = 2$–8 T), high density ($n_{LCFS} \sim 0.2$–1×10^{20} m^{-3}) device with major radius $R_0 = 0.67$, minor radius $a = 0.2$ m, and metallic walls. We concentrate on a series of Ohmic, limited discharges that were used to assess the ITER limiter re-design.[1] The toroidal field was 4 to 6.5 T, the plasma current was 0.4 to 1 MA, and the vertical elongation at the LCFS was $\kappa = 1.2$. The plasma density was kept around $0.2 < n/n_{GW} < 0.35$.

One of the experimental objectives was to extract a dependence of λ_q on the plasma parameters. A narrow feature was found in all of the discharges using three Langmuir probes at different poloidal angles. The narrow-feature λ_q was of the order of 1–5 mm, with a far SOL $\lambda_{q,main}$ about a factor of 5–10 longer. The peak heat flux at the LCFS is about 4 times larger than a single exponential fit based on the far SOL profiles would predict. It was found that λ_q scaled roughly inversely with the plasma current (or proportionally to the safety factor), without any significant sensitivity to other plasma parameters. The measured λ_qs are similar to those predicted by Goldston's heuristic drift model.[13]

From all the discharges carried out, we discuss two cases that were specifically run for comparison against GBS simulations. As mentioned before, $\lambda_q \sim B_{\theta,OMP}^{-1}$, without any significant variation of λ_q with respect to other parameters. The two simulated scenarios result from a composite of a few discharges carried out at $B = 4.1$ T, with safety factors $q_a \approx 2.75$ and $q_a \approx 4.25$. The temperature at the LCFS was about 40 eV and (based on measurements in similar discharges) the ion temperature was about twice as high, which results in an ion sound gyroradius of about 0.4 mm. The main plasma parameters and discharge numbers are shown in Table I. Just below, we give a short description of the diagnostic capabilities used for the study.

A. Mirror Langmuir probe

C-Mod has an array of three Langmuir probes: (a) an electromagnetically actuated wall probe (WASP)[28] near the

TABLE I. Numerical parameters used in GBS simulations.

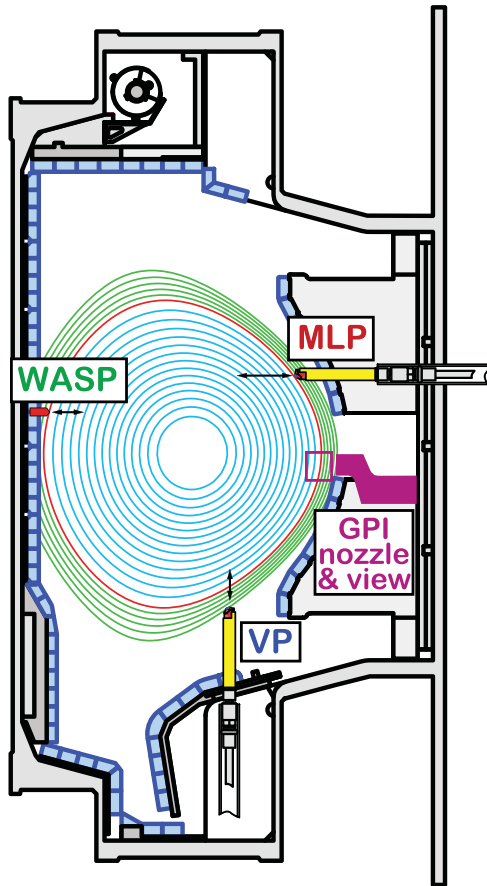| Discharges	B_T (T)	I_p (MA)	$n_{e,LCFS}$ (m^{-3})	$T_{e,LCFS}$ (eV)	q_a
1140619002/03/04	4.1	0.7	0.3×10^{20}	40	2.75
1140619008/11	4.1	0.4	0.3×10^{20}	40	4.24

FIG. 1. Schematic of Alcator C-Mod showing the locations of the Langmuir probe and gas-puff imaging (GPI) diagnostics. The magnetic flux surfaces for discharge 1140619011 ($I_p = 0.4$ MA case) are displayed. The present paper concentrates on outer midplane profile and turbulence data from the mirror Langmuir probe (MLP) and the GPI views.

contact point in the inner-wall, (b) a Mirror Langmuir probe around the outer midplane,[29] and (c) a vertical probe (VP) plunging from below the equatorial midplane. A schematic of C-Mod showing the locations of the probes is shown in Fig. 1. The present study concentrates on data acquired with the MLP at the outer midplane. Its design and the acquisition and analysis techniques are described in detail in Ref. 29. The principal advantage of the C-Mod MLP with respect to conventional Langmuir probes is that it can acquire SOL profiles at high spatial and temporal resolution, allowing in fact simultaneous measurements of density, temperature, and floating potential in the typical turbulence timescale, ~ 1 μs. Figure 2 shows the density, temperature, floating potential, and plasma potential $\phi \approx V_{fl} + 2.5 T_e / e$ profiles obtained from the MLP in discharge 1140619004. We show a composite mean profile combining four tip probes and smoothing over 200 μs, as well as the raw data from the North East (NE) probe tip. The two lines correspond to the inner and outer strokes of the reciprocation. Reconstruction of the magnetic flux surfaces from magnetic measurements is able to deduce the location of the last closed flux surface only within approximately 5 mm. On diverted discharges, electron temperature profile measurements combined with power balance analysis can be used to identify the location of LCFS within about 1 mm.[29] It is found that the plasma potential roughly peaks at the LCFS location. Based on this guidance, the profiles in these inner-wall limited plasmas have been shifted to put the plasma potential maximum at the LCFS, which is indicated as a dashed line in Fig. 2. The n_e and T_e profiles have a near-SOL exponential decay length of the order of 3–5 mm.

It is also noted the MLP, WASP, and VP have all shown a two decay-length structure with little variation in the
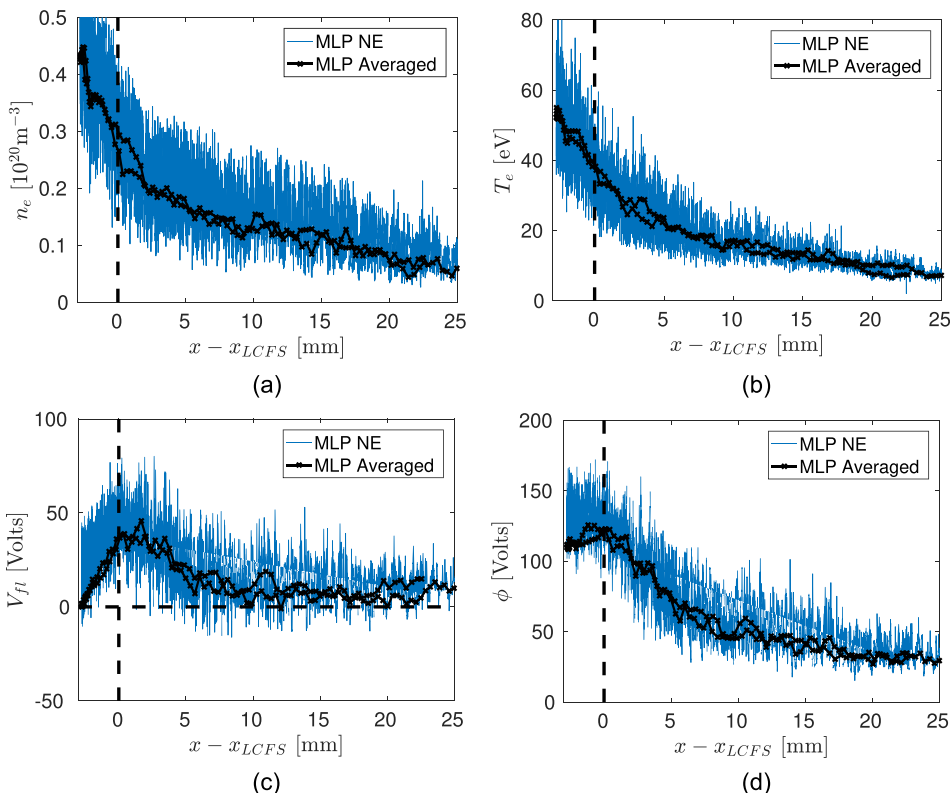

FIG. 2. Density, temperature, potential, and floating potential profiles as measured by the MLP in CMOD discharge 1140619004. Each plot shows the raw signal from the North East (NE) probe tips, as well as a composite mean profile.

plasma profiles along the poloidal angle.[7] Thus, it appears that the plasma gradients along the magnetic field line, as inferred from Langmuir probe (LP) data, are negligible. This is not the case in other devices, such as DIII-D and COMPASS,[6,30] where the narrow feature is either weak or undetectable on the low field side (LFS). Nevertheless, the lack of poloidal gradients in C-Mod IWL scenarios is consistent with the target scenario for the experiments being sheath-limited plasmas. As GBS simulations typically show weak parallel gradients, the plasma properties further encourage a detailed comparison of MLP data and GBS results.

B. GPI diagnostic

The C-Mod GPI diagnostic is described in detail in Ref. 31. The diagnostic measures visible light fluctuations resulting from a localized helium gas puff. The GPI system used for this paper consists of a 2D array of 9×10 discrete views of the local gas puff, each with a 3.8 mm viewing diameter, placed on the outer equatorial midplane. The views are coupled via fibers to arrays of Avalanche Photo Diodes (APDs). The measured light emission is dependent on the density and temperature fluctuations. In fact, the GPI light emissivity is modeled in GBS as $\delta I / \langle I \rangle \sim n^\alpha T^\beta$, with α and β based on the atomics physics data used in DEGAS-2 simulations.[32] The GBS RMS/mean density and temperature fluctuations are of similar magnitude as the simulated GPI fluctuations.

Several pixels of the GPI array were defective during the 2014 campaign and have been excluded from the analysis. A simulated GPI emissivity is reconstructed from the GBS results using the methods described in Refs. 10 and 23, however, using the 2D viewing geometry of the APD system. The light fluctuations are well correlated with density and temperature fluctuations. The GPI system is suited to characterize macroscopic turbulent features, such as correlation lengths and propagation velocities. It is also capable of extracting geometric features such as the tilt and ellipticity of the turbulent structures.

Spatial smoothing must be taken into account in the GPI reconstruction in GBS. Besides the 3.8 mm spatial resolution of the detectors, the angle between the GPI viewing chords and the magnetic field lines (due to magnetic field line tilt) must be taken into account. DEGAS-2 neutral transport calculations including atomic physics have been carried out to determine the extent of the light emission from the localized gas puff, in order to account for this effect. The poloidal smoothing is about 8 mm for the $q_a = 2.75$ case, and about 6 mm for the $q_a = 4.25$ case. Hence, as in our previous work, the extension of the gas puff dominates the poloidal resolution, and there is a sharp cutoff of the GBS simulated GPI signal for wavenumbers above 1 cm^{-1}.

III. SIMULATIONS OF THE ALCATOR C-MOD SOL

A. Model equations

The turbulent dynamics of the C-Mod IWL SOL is modeled with the GBS code,[8,9] a thoroughly verified[33] and validated[34] 3D non-linear flux-driven code based on the drift-reduced Braginskii system of equations,[35] including the possibility of evolving a single neutral atomic species.[36] The physical model derives from applying the orderings $d/dt \ll \omega_{ci}$ ($\omega_{ci} = eB/m_i$ is the ion gyrofrequency) and $k_\perp \gg k_\parallel$ to the Braginskii fluid equations[37] and is appropriate to study the non-linear dynamics of low frequency, low wavenumber drift, and ballooning-type turbulence. The simulations do not differentiate between background and fluctuations, and thus the plasma profiles are a result of the simulated plasma dynamics. Codes such as BOUT++ (Ref. 38) and TOKAM3X[39] allow for similar physical and numerical capabilities as GBS. The dynamics of blob filaments simulated in these codes was recently compared under tokamak relevant conditions.[26]

We find that a simple five-field fluid model that neglects ion temperature and uses the Boussinesq approximation ($\nabla \cdot (\partial_t n \nabla_\perp \phi) \approx n \partial_t \nabla_\perp^2 \phi$) can capture the profile steepening found in C-Mod. Simulations removing the Boussinesq approximation and including a thermal ion species are have been carried out for generic IWL plasmas, without dramatic consequences for the turbulence dynamics.[40] The ion temperature has been shown to slightly enhance the ballooning drive, as well as having effects upon filament motion.[41,42] A lock-in mechanism between T_i and ϕ through the vorticity equation, which can affect the electric field within the confined region,[43] is also neglected.

Additionally, since the C-Mod discharges have weak poloidal plasma gradients, we have omitted the effects of neutrals for computational purposes. The neutral model implemented in GBS has not been parallelized yet to the plasma sizes required for C-Mod comparison, due to the spatial non-locality of the kinetic kernel functions describing neutral plasma interaction.[36] For an attached plasma with weak poloidal plasma gradients, a temperature sink near the limiter due to the interaction with neutrals would have the effect of decreasing the temperature along the entire field line. However, as the parallel transport is dominated by convection, there would be a negligible effect on the perpendicular decay lengths.

The model equations for conservation of density n, vorticity $\Omega = \nabla_\perp^2 \phi$, parallel electron and ion velocities $v_{\parallel e,i}$, and electron temperature T_e read

$$\frac{dn}{dt} = \frac{2}{eB} \left[\hat{C}(p_e) - en\hat{C}(\phi) \right] - \nabla \cdot \left(nv_{\parallel e} \hat{\mathbf{b}} \right) + D_n \nabla_\perp^2 n + S_n,$$

$$(1)$$

$$\frac{d\Omega}{dt} = \frac{2B}{nm_i} \hat{C}(p_e) + \frac{B^2}{nm_i} \nabla \cdot \left(j_\parallel \hat{\mathbf{b}} \right) - v_{\parallel i} \nabla_\parallel \Omega + D_\Omega \nabla_\perp^2 \Omega$$
$$+ \frac{B}{3nm_i} \hat{C}(G_i),$$

$$(2)$$

$$\frac{dv_{\parallel e}}{dt} = \frac{ej_\parallel}{\sigma_\parallel m_e} + \frac{e\nabla_\parallel \phi}{m_e} - \frac{\nabla_\parallel p_e}{nm_e} - \frac{0.71\nabla_\parallel T_e}{m_e} - v_{\parallel e} \nabla_\parallel v_{\parallel e}$$
$$+ D_{v_{\parallel e}} \nabla_\perp^2 v_{\parallel e} - \frac{2\nabla_\parallel G_e}{3nm_e},$$

$$(3)$$

$$\frac{dv_{\parallel i}}{dt} = -\frac{\nabla_\parallel p_e}{n} - v_{\parallel i} \nabla_\parallel v_{\parallel i} + D_{v_{\parallel i}} \nabla_\perp^2 v_{\parallel i} - \frac{2\nabla_\parallel G_i}{3nm_i}, \quad (4)$$

$$\frac{dT_e}{dt} = \frac{4}{3}\frac{T_e}{eB}\left[\frac{7}{2}\hat{C}(T_e) + \frac{T_e}{n}\hat{C}(n) - e\hat{C}(\phi)\right]$$
$$+ \frac{2T_e}{3en}\left[0.71\nabla\cdot\left(j_{\parallel}\hat{\mathbf{b}}\right) - en\nabla\cdot\left(v_{\parallel,e}\hat{\mathbf{b}}\right)\right]$$
$$- v_{\parallel e}\nabla_{\parallel}T_e + \chi_{\perp,e}\nabla_{\perp}^2 T_e + \chi_{\parallel,e}\nabla_{\parallel}^2 T_e + S_{T_e}. \quad (5)$$

In these equations, $df/dt = \partial f/\partial t + \{\phi,f\}/B$, we use the Poisson bracket $\{g,f\} = \hat{\mathbf{b}}\cdot(\nabla g \times \nabla f)$ and the curvature operator $\hat{C}(f) = (B/2)(\nabla\times(\hat{\mathbf{b}}/B))\cdot\nabla f$. The unit magnetic field vector is $\hat{\mathbf{b}} = \mathbf{B}/B$, $j_{\parallel} = en(v_{\parallel i} - v_e)$ is the parallel current, and $\sigma_{\parallel}$ is the Spitzer conductivity. The coordinate system is given by the poloidal length, radial, and toroidal angle coordinates ($y = \theta a, x, \varphi$). S_{T_e} and S_n represent source terms used to inject density and temperature into the simulation domain. The numerical implementation of Eqs. (1)–(5), including the definition of the gyro viscous terms $\sim G_{e,i}$ and other dissipative contributions, is described in detail in Ref. 9. The dissipative contributions (D_n, D_{Ω}, etc.) are introduced to control numerical pile-up at wavenumbers approaching or exceeding the grid resolution. The numerical transport coefficients were set to a constant value of 2. Using a simple 1D transport code, we have verified that the profiles resulting from a balance between the source terms, the numerical diffusion, and an approximate form of the parallel convection have decay lengths of $2\rho_s$, which is less than 1 mm in C-Mod. Therefore, the transport dynamics are dominated by the turbulence rather than by the sources.

B. Simulation setup

Two simulations are carried out using the parameters given in Table II. Although the ion temperature is not evolved, we use its reference value at the LCFS to evaluate the dimensionless plasma size $\rho_{\star} = \rho_s/R$. The radial, poloidal, and toroidal grids have $n_x = 127$, $n_y = 1407$ or 2175, and $n_z = 256$ points, which nears the limit of the present parallel scalability of the GBS code. The poloidal grid resolution is about 0.5 mm, compared to turbulent filament sizes of about 2 cm. The simulated radial region ($-20\rho_s < x < 80\rho_s$) is roughly 2.5 cm, compared to a 2 cm gap between the LCFS and outer poloidal limiter in the C-Mod discharges.

It is worth discussing the role of boundary conditions and plasma sources in the simulations. The poloidal domain is bounded by a simulated infinitely thin toroidal limiter, where we apply Loizu's fluid model for the Bohm-Chodura sheath.[44] The toroidal limiter plays the role of C-Mod's inner-wall. Including a realistic boundary would slightly decrease the connection length by restricting the poloidal extension of the plasma by a few degrees, in particular in the far-SOL.

TABLE II. Grid resolution and numerical parameters used in GBS simulations.

Discharge	n_x	n_y	n_z	L_y	m_i/m_e	A_n	A_{T_e}	$\sigma_{n,T}$
1140619004	127	1407	256	3200	1600	1.8	1.6	2.5
1140619011	127	2175	256	3200	1600	1.0	1.0	2.5

The radial boundary conditions are $\partial_x T_e = \partial_x n = \partial_x v_{\parallel i,e} = 0$. The potential function ϕ is set to $\partial_x\phi = 0$ at the inner boundary and to $\Lambda\langle T_e\rangle_t$ at the wall ($\Lambda = \log\sqrt{m_i/(2\pi m_e)} \approx 3$, and the angled brackets $\langle\rangle_t$ denote time averaging). For $x > 70\rho_s$, we impose a $10\rho_s$ radial buffer layer where the vorticity Ω is slowly evolved towards 0. The buffer region is useful for numerical purposes, since advecting large coherent structures through the boundary can be demanding.

In the present simulation setup, the S_n and S_{T_e} terms in Eqs. (1) and (5) emulate plasma outflowing from the confined region, i.e., the plasma edge. The sources are described by the expression $S = A\exp\left(-(x-x_0)^2/\sigma^2\right)$, with $A_n \approx 1$, $A_{T_e} = \approx 1$, $x_0 = 20\rho_s$, and $\sigma = 2.5\rho_s \approx 1$ mm. The source intensity is regulated such that the reference n and T_e match the LCFS experimental values. Our analysis interprets the source radial location x_0 as the LCFS, and we analyze the radial domain between x_0 and the location of the outer vorticity sink, $x = 70\rho_s$. The width of this region is a good match for the 2 cm gap between the LCFS and the outer poloidal limiter in C-Mod.

The temperature profile peaks at the source injection point, affecting the potential. Since the electrostatic potential is closely coupled to T_e through the Bohm sheath condition, the poloidal $\mathbf{E}\times\mathbf{B}$ velocity changes sign around the source. Consequently, the source has a side effect of creating a shear layer at the injection point. Note, however, that the potential profiles are consistent with the definition of the LCFS used for the probe measurements. We have found that such a shear layer can arise spontaneously in GBS simulations with open and closed magnetic field lines.[45]

The sheath boundary conditions play an important physical role in steepening the plasma profiles. Loizu's fluid sheath model allows currents flowing at the target plates, and an interaction between these currents and the turbulence takes place in GBS simulations. The turbulent intensity has a radial gradient, which in turn drives non-ambipolar currents at the sheath. These currents allow the potential to deviate from its floating value $\sim\Lambda T_e$. The electric potential drops significantly at the LCFS with respect to its floating value, in effect driving an $\mathbf{E}\times\mathbf{B}$ shear layer. This physical mechanism has been shown to predict the narrow-feature λ_q in GBS simulations with open and closed magnetic field lines.[45]

C. GBS output analysis

For comparison with the C-Mod experiments, we consider a reconstruction of the HeI (587.6 nm) line emission intensity using the simulated n and T_e. The principal assumption is that the fluctuations in the light emission intensity can be approximated as $\delta I/I \approx \alpha\delta n/n + \beta\delta T_e/T_e$ by expanding the n^{α} and T_e^{β} dependence about their time-averaged values. In order to match the GPI space and time resolution, we employ a moving average filter with a 3×3 mm resolution, with an additional 6–8 mm smoothing to simulate the effects of the magnetic field line tilt. This approach has been used in Refs. 10, 18, and 23 and is based on DEGAS2 modeling of the neutral gas puff cloud evolution.[46] The influence of spatial smoothing is shown in Fig. 1 of Ref. 10—structures with a wavenumber comparable to ρ_s^{-1} are strongly smoothed,

which nevertheless does not affect the evaluation of the macroscopic characteristics of the turbulent filaments with $k_\perp \rho_s \approx 0.1$.

Using the GPI signals, we have evaluated correlation lengths, mode ellipticity, and tilt by building 2D cross-correlation functions centered around each GPI pixel. The cross-correlation function is then interpolated to a finer grid using cubic splines, and a tilted ellipse is fitted to the contour where the correlation falls to 0.7 (see Fig. 3). The poloidal and radial correlation lengths, L_{pol} and L_{rad}, are obtained from the vertical and horizontal lengths of the ellipse; the ellipticity is L_{pol}/L_{rad}, and the tilt is obtained from the position of the semi-major axes of the ellipse. The same analysis technique is employed for the C-Mod GPI and for the simulated GBS GPI.

In order to evaluate the radial profiles of the turbulence phase velocity, two analysis methods were used. One (FA) uses Fourier analysis in time and in the poloidal spatial dimension and assumes that the radial phase velocity is small compared to the poloidal velocity. The second method uses a Time-Delay Analysis (TDE) and filters signals in time using a hi-pass filter at 30 kHz. Both methods typically agree well with the MLP phase velocity profiles. We display the results of the high-pass TDE analysis. The GPI profiles have been shifted outwards by 3 mm to match the MLP profiles, using the change in the phase velocity sign from electron to ion diamagnetic direction, which typically takes place near the LCFS.

In the GBS simulations, the length of the time series (<1 ms) was too short to allow a precise evaluation of the velocities using this method. For this reason, we have tracked the 2D trajectories of the large amplitude turbulent filaments (blobs) within the poloidal plane. We considered a detection threshold of $\delta n/\langle n \rangle = 2.5$ and computed the velocities using the center of mass position vs. time of 1500 filaments. This was carried out using the plasma density, without smoothing the signal to simulate the GPI resolution and tilt with respect to the magnetic field lines.

The C-Mod MLP measurements are compared against a time and spatial average of GBS density and temperature data from the outer midplane. This simplification is justified in the discharges studied, since C-Mod measurements in
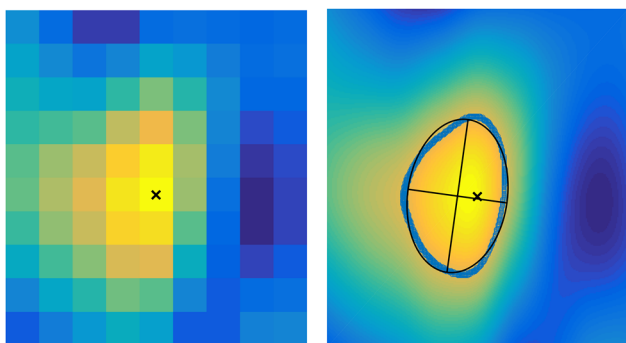

FIG. 3. Left: Cross-correlation coefficients between pixel (5, 5) (marked with a cross) and the other sensors. Right: Interpolated 2D cross-correlation function used to determine L_{pol}, L_{rad}, mode ellipticity, and tilt. The blue line indicates the position where the correlation drops to 0.7, which is fitted with a tilted ellipse (black line).

IWL discharges are similar as a function of the poloidal angle within a flux-surface. Recent work with TOKAM3D attempts to model the effects of a biased LP within the context of a 3D fluid model, finding that some perturbative effect from the LP onto the turbulence is possible.[47] We have not attempted to simulate the LP perturbative effect. The GBS data are spatially and time averaged in order to increase the smoothness and robustness of the profiles, as the simulated time, of the order of 1 ms, is much shorter than the either MLP reciprocation or the GPI acquisition time.

IV. COMPARISON BETWEEN C-MOD DATA AND GBS SIMULATIONS

The experiment-simulation comparison is carried out in the following context. We are interested in establishing relationships between the narrow feature profiles and the turbulent properties of the SOL. The quantities of interest are those that can be used to determine the cross field turbulent transport levels, e.g., the plasma gradients, the fluctuation moments (amplitude, skewness), the correlation lengths and time, and the filament velocity. In addition, recent publications (e.g., Refs. 1, 4, and 13) have attempted to interpret the narrow feature decay length as arising from neoclassical processes, which are not included in GBS. Therefore, it is of interest to search and understand plasma conditions under which turbulent transport is normally believed to be suppressed, e.g., strong flow shear layers. These results follow below.

A. Plasma profiles

The simulated plasma profiles are compared against C-Mod data in Fig. 4 (top: n_e, center: T_e, bottom: plasma potential ϕ). The radial coordinate is defined with respect to the LCFS, which is found in C-Mod by shifting the potential profile to its maximum. The GBS profiles set the LCFS as the location of a plasma source mimicking plasma outflow into the open magnetic field line region. The absolute value of n_e and T_e at the LCFS is reasonably matched by the GBS simulations—this is achieved by numerically adjusting the source terms. The GBS profiles are obtained from time and toroidal averaging over the low-field side. However, the simulated plasma profiles are essentially poloidally uniform. On the bottom right panel of the figure, we observe a large mismatch between the plasma potentials, which is due to a strong deviation from the floating potential $\Lambda T_e \approx 120$ V near the LCFS found in the MLP data. The GBS simulations do not capture the large deviation from the floating potential observed in the experiment.

The MLP profiles show a break in gradient steepness about 3–5 mm outside the LCFS. The GBS simulations have a noticeably weaker narrow feature, which is nonetheless easily recovered by fitting the profiles. The model used to fit the density and temperature profiles reads, for a given scalar f,

$$f(x) \propto R \exp(-x/L_f) + \exp(-x/L_{f,main}), \quad (6)$$

with the x coordinate centered at the LCFS. The fit is carried out using a nonlinear fitting routine to determine the
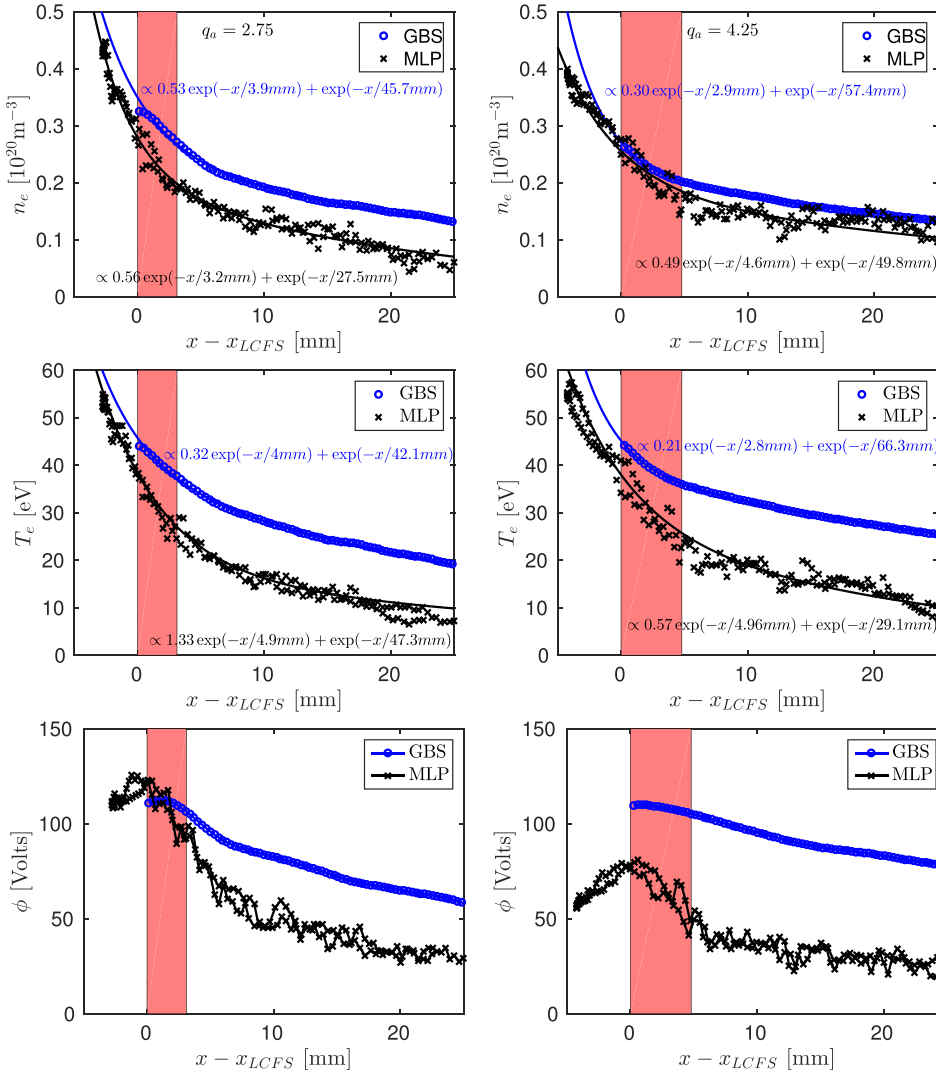
FIG. 4. MLP and GBS plasma profiles (top: n_e, center: T_e, bottom plasma potential ϕ) for $q_a = 2.75$ case (left) and $q_a = 4.25$ case (right). The MLP profiles are shown as black lines with-×s, while the GBS profiles are shown as blue lines with open circles. The shaded areas indicate the width of the steep gradient region obtained from fitting the experimental density profiles with Eq. (6).

coefficients R, L_f, and $L_{f,main}$ from the LCFS up to the outer wall. The decay lengths L and L_{main} correspond to the near and far SOL, while the constant R indicates the strength of the narrow feature relative to the far SOL decay. Both MLP data and GBS simulations yield near-SOL gradient lengths of the order of 3–5 mm, while the far-SOL profiles have characteristic lengths of 25–50 mm. The 95% confidence interval for the fits to the MLP data is roughly 1 mm for the near SOL profiles and 1 cm for the far SOL profiles. The fits to the GBS profiles result in narrower confidence intervals (0.5 and 5 mm) compared to the MLP fits. One of the GBS temperature profiles has $L_{T_e,main} = 151$ mm, which is essentially a flat profile if compared with the 25 mm gap. As anticipated from the figure, the value of $R \approx 1$ is significantly larger in the MLP data than in the GBS simulations ($R \approx 0.3$). Most of the MLP-GBS disagreement stems from the small R factor in the GBS simulations with respect to the flat exponential profiles. The profile gradients and fitting constants for n_e and T_e, as defined in Eq. (6), are shown in Table III. The R factors found in the experimental data are similar to those found in DIII-D IWL discharges using a HFS swing probe.[6] However, the edge Thomson scattering diagnostic data from the same DIII-D discharges did not always find profile steepening near the separatrix.

The MLP plasma potential profiles are strongly peaked near the LCFS, indicating a strongly varying poloidal $\mathbf{E} \times \mathbf{B}$ velocity at the interface between the SOL and the confined region. Figure 5 shows the shearing rate $\gamma_{\mathbf{E} \times \mathbf{B}}$ and compares it to an approximation to the reference ballooning growth rate γ_b. The following definitions are used:

TABLE III. Characteristic decay lengths L, L_{main}, and narrow feature strength factor R obtained from non-linear fit to a double exponential function $f(x) \propto R \exp(-x/L) + \exp(-x/L_{main})$. Typical fit uncertainties for the near and far-SOL decay lengths are, respectively ± 1 mm and ± 10 mm for the MLP data; and ± 0.5 mm and ± 10 mm for the GBS simulations (indicated for the density decay length in the $q_a = 2.75$ case).

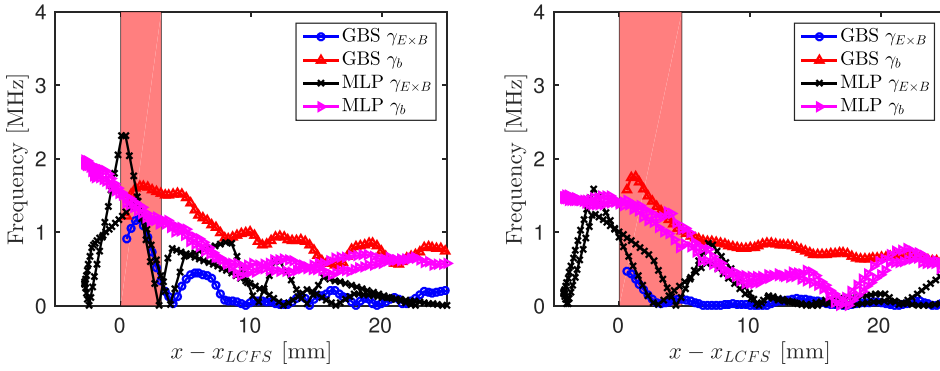| Discharge		1140619004		1140619011	
I_p	(MA)	0.7		0.4	
q_a		2.75		4.25	
		MLP	GBS	MLP	GBS
R_{n_e}		0.56	0.53	0.49	0.30
L_{n_e}	(mm)	3.2 ± 1	3.9 ±0.5	4.6	2.9
$L_{n_e,main}$	(mm)	27.5 ± 10	45.7 ± 5	49.8	57.4
R_{T_e}		1.3	0.32	0.57	0.21
L_{T_e}	(mm)	4.9	4.0	4.96	2.8
$L_{T_e,main}$	(mm)	47.3	42.1	29.1	66.3

FIG. 5. Velocity shear and reference interchange growth rates computed from the MLP and GBS plasma profiles for $q_a = 2.75$ case (left) and $q_a = 4.25$ case (right).

$$\gamma_{\mathbf{E}\times\mathbf{B}} \approx \frac{1}{B_{OMP}} \frac{\partial^2 \phi}{\partial x^2}, \tag{7}$$

$$\gamma_b = c_s \sqrt{\frac{-2}{R_0 p_e} \frac{\partial p_e}{\partial x}}, \tag{8}$$

with $B_{OMP} \approx B_0/(1 + a/R_0) = 3.15\,\mathrm{T}$ being used as an approximation to the magnetic field strength at the LCFS. In Eq. (7), we neglect the radial variation of B_{OMP}, which over a 2 cm distance is small compared to the potential drop. Likewise, γ_b is an approximation to the ballooning growth rate and it is shown as an upper bound to the turbulent growth rate in the absence of sheared flows. The actual linear growth rates depend on other factors (principally, the Spitzer resistivity, flux-surface shaping, and the magnetic shear). Typical growth rates for resistive ballooning modes in the low wavenumber spectrum, where non-linear turbulence is observed in GBS simulations, are about $\gamma_b/2$ or less.[48]

In both discharges, the MLP profiles reveal the presence of shear rates of the order of the linear growth rate. It must be noted, however, that no clear connection has been shown so far between tokamak edge turbulence levels and the local shear rate in limited plasmas. The far SOL, on the other hand, has $\gamma_{\mathbf{E}\times\mathbf{B}} \ll \gamma_b$, and thus we would expect strong interchange turbulence. The break in profile steepness observed 5 mm outside the LCFS corresponds to $\gamma_{\mathbf{E}\times\mathbf{B}}$ falling well below γ_b. The GBS simulations show a similar qualitative behavior, although $\gamma_{\mathbf{E}\times\mathbf{B}}$ remains smaller than γ_b, in particular in the simulation of the $q_a = 4.25$ scenario. In effect, we observe $\gamma_{\mathbf{E}\times\mathbf{B},GBS} \approx \gamma_{\mathbf{E}\times\mathbf{B},MLP}/2$. Hence, the weakness of the shear layer in GBS simulations is the one plausible explanation for the weak R factors in Table III. In effect,

experimental data from TCV have shown that R increases as V_{fl} at the separatrix (itself related to the shear rate) deviates from ground.[49] However, other causes such as increased filament propagation speed widening the SOL cannot be ruled out. The numerical dissipative terms D_n, D_Ω, and χ_e can also increase λ_q through particle and heat diffusion, and by damping the flow vorticity. However, this effect appears to be of the order of 1 mm or less, according to an evaluation of the profiles carried out in a simple 1D transport code with constant transport coefficients and an approximate form of the parallel loss term $\propto c_s/(q_a R_0)$. Varying the value of D_n, D_Ω, and χ_e between 10 and 2 in GBS simulations typically increases $\gamma_{\mathbf{E}\times\mathbf{B}}$ modestly around the LCFS and shortens λ_q by $1\text{--}2\rho_s$, the latter figure being essentially within the uncertainty of the fitting procedure.

B. Fluctuation levels and intermittency

The objective of this subsection is to characterize the turbulent behavior, in particular, in the context of the shear layer found in the MLP data and in the GBS simulations. We concentrate on two moments of the fluctuation distribution function: the RMS/mean fluctuation level (left) and the skewness (right), shown in Fig. 6 for the $q_a = 4.25$ case. Note that, since the GPI emission responds to both density and temperature fluctuations, the MLP and GPI profiles need not match.

Relative fluctuation levels of 0.1–0.25 persist in the near-SOL even in the presence of the shear layer. While the RMS/mean level observed with the MLP is smaller in the near-SOL than in the far-SOL, the relative GPI light fluctuations are maximum around the LCFS. GBS simulations show the opposite trends: density fluctuations are maximum near the LCFS and decrease with radius, while the simulated GPI
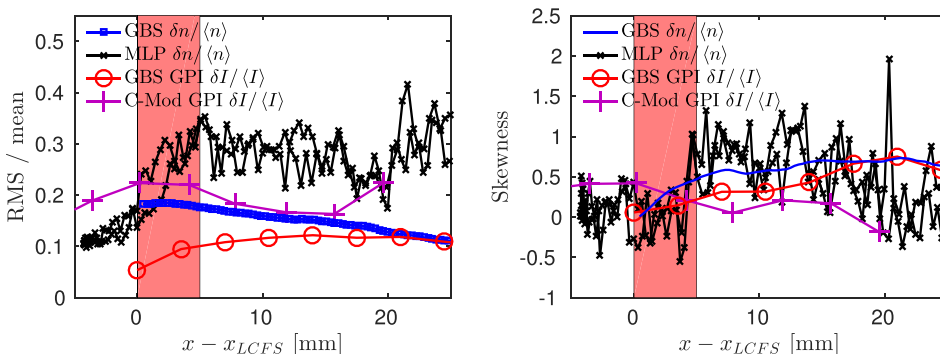

FIG. 6. RMS fluctuation level (left) and skewness (right) as a function of radius in the $q_a = 4.25$ case.
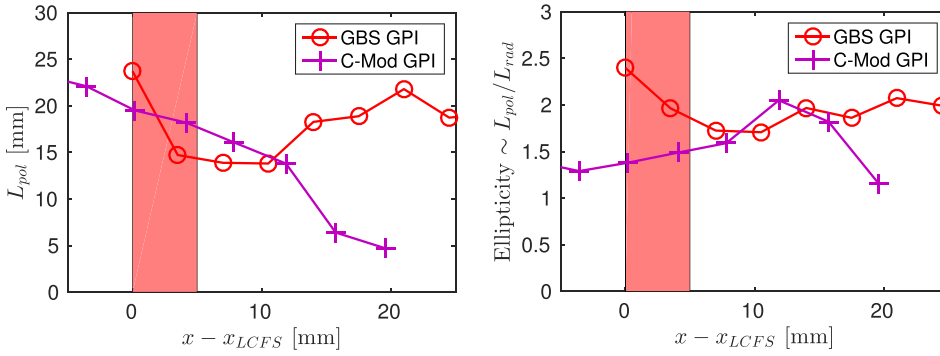
FIG. 7. Poloidal correlation length and model ellipticity L_{pol}/L_{rad} obtained from GBS simulations (red circles) and the C-Mod GPI data (magenta crosses) in the $q_a = 4.25$ case.

fluctuations are minimum within the shear layer. Altogether, the GBS simulation finds a relative density fluctuation that is roughly half that found with the probe, while in the far SOL, the synthetic GPI fluctuation from the simulation is roughly that measured. Thus, our comparison neither supports nor rules out decreased turbulent amplitude within the shear layer as the profile steepening mechanism. Similar results were found for the $q_a = 2.75$ case.

The left panel of the figure shows the normalized fluctuation moments for density ($\delta n/\langle n \rangle$) and HeI emissivity ($\delta I/\langle I \rangle$). The GPI and MLP measurements match very well around the LCFS, showing a fluctuation amplitude of the order of 10%–15%. The GBS simulations show a similar fluctuation level, although the simulated GPI signal indicates a slightly lower $\delta I/\langle I \rangle$. While the relative fluctuation level observed with the MLP increases away from the separatrix, the *absolute* fluctuation level (e.g., $n - \langle n \rangle$) remains roughly constant.

The $\delta n/\langle n \rangle$ and $\delta I/\langle I \rangle$ skewness profiles are shown on the right panel of Fig. 6. The skewness ranges between ± 0.5 for the MLP data. All of the signals indicate negligible skewness near the LCFS, i.e., Gaussian transport statistics, with the intermittency level rising further away from the separatrix. This behavior is exactly as expected: blobs originate near the separatrix and they have a considerable effect on radial transport in the far SOL. The presence of a shear layer in the narrow feature is consistent with theories and observations, affirming that blobs detach from interchange instabilities sheared by poloidal $\mathbf{E} \times \mathbf{B}$ flows.[22,50,51]

C. Correlation lengths

The correlation lengths were evaluated using the C-Mod GPI and the simulated GPI using the procedure outlined in Sec. III C. We show the correlation length and the mode ellipticity for the $q_a = 4.25$ case in Fig. 7. The poloidal correlation length is of the order of 15–20 mm at the LCFS and decreasing away from the separatrix. The ellipticity $L_{pol}/L_{rad} \approx 2$ is about constant throughout the SOL. Thus, it must be pointed out that the mesoscale estimate for the radial correlation length,[52] $1/L_{rad} \sim \sqrt{1/(L_{pol}L_p)}$, does not reproduce the observed experimental trends. If the mesoscale estimate applied, one would expect that L_{rad} increases away from the separatrix (decreased ellipticity), while in fact the ellipticity remains constant and both L_{rad} and L_{pol} decrease.

The ellipse fitted to the 2D correlation functions provides additional information, such as the mode size (area) and tilt. Since the correlation lengths are well reproduced by the GBS simulations in the near-SOL, the area is recovered as well. Generally, tilting could result either from radially sheared poloidal flows or from shear in the magnetic field line pitch across the flux surfaces. In the C-Mod data, the tilt is small ($<20°$) in the $q_a = 2.75$ case and is larger, and switching from positive to negative, in the $q_a = 4.25$ case. The ellipses fitted to the GBS simulated GPI always show little to no tilting ($<10°$ mode tilt). Thus, this aspect of the comparison is inconclusive and should be reconsidered using more realistic geometry in GBS (e.g., closed flux surfaces, global magnetic equilibrium, reversed magnetic field) in order to better capture the effects of sheared flows and magnetic field.

D. Phase and drift propagation velocities

The left panel of Fig. 8 shows the phase propagation velocities measured in C-Mod for the $q_a = 4.25$ case. The MLP phase velocity is obtained from the delay that maximizes cross-correlation between the "north" and "south" probe tips. The positive direction is determined by the
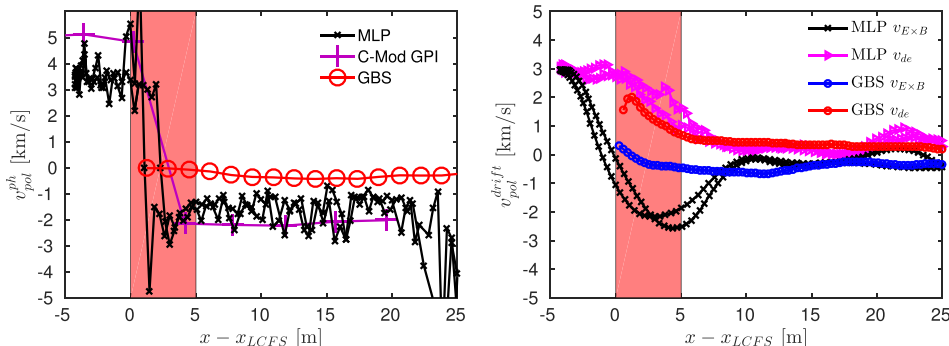

FIG. 8. Poloidal velocity profiles for C-Mod MLP and GPI data (left) and for GBS simulation in the high q case. The direction of filament motion (down in C-Mod, up in GBS) is due to the toroidal magnetic field being reversed in the GBS simulations with respect to C-Mod.

electron diamagnetic drift direction, with the same convention applied to the MLP, GPI, and GBS data. The MLP and GPI signals agree well across the profile, after aligning the profiles to the radial location where the poloidal velocity switches from electron to ion diamagnetic drift direction. The turbulence poloidal velocity is in the range of 1–2 km/s, with a change in the direction of propagation near the LCFS. These values are within the same range as those found in diverted C-Mod discharges.[53] In the GBS simulations, mode velocities were extracted from the filament center-of-mass positions. Altogether, we tracked 1500 blob filaments for each simulation, and the velocities shown are an ensemble average giving each filament equal weight regardless of its size. The poloidal velocity is approximately –300 m/s, smaller in magnitude than the velocities measured by the MLP and GPI diagnostics. The radial velocity found in GBS for the high-q_a case is of the order of 400 m/s, while the GPI diagnostic has $v_{rad} \approx -400 \pm 400$ m/s.

The $\mathbf{E} \times \mathbf{B}$ and diamagnetic drift velocities (shown on the right panel of Fig. 8) are evaluated from the following formulas:

$$v_{\mathbf{E}\times\mathbf{B}} = \frac{\hat{\mathbf{b}}}{B} \times \frac{\partial \phi}{\partial x}, \tag{9}$$

$$v_{de} = -\frac{\hat{\mathbf{b}}}{e n_e B} \times \frac{\partial (n_e T_e)}{\partial x}. \tag{10}$$

The poloidal $\mathbf{E} \times \mathbf{B}$ drifts obtained from the MLP are of the order of –1–2 km/s in the near SOL, in the same order of magnitude as the poloidal phase velocity. The $\mathbf{E} \times \mathbf{B}$ drift velocity obtained from GBS is significantly smaller in magnitude, in part due to the weaker radial profile gradients. The diamagnetic speed, which stems from the pressure gradient, is well reproduced. We have also computed phase and drift velocities for the $q_a = 2.75$ case, which were similar to the ones shown.

V. SUMMARY AND CONCLUSIONS

We present a comparison between non-linear flux driven turbulence simulations of the C-Mod SOL dynamics, carried out with GBS, and high resolution MLP and GPI measurements of the plasma profiles and fluctuations. The comparison is based upon L-mode inner-wall limited discharges carried out to determine the parametric scaling of the near-SOL heat-flux decay widths.[1] MLP data revealed steep profile gradients just outside the LCFS. We concentrated on two discharges with $B = 4$ T at $I_p = 0.7$ MA and $I_p = 0.4$ MA and $q_a = 2.75$ and $q_a = 4.25$, respectively.

While in a previous publication[10] we concentrated on "bulk" estimates of the fluctuation moments and correlation lengths averaged across the far SOL, recent advances in diagnostics have allowed us to investigate the plasma profiles and the variation of the turbulent characteristics as a function of the SOL radius. The two-fold objective, attempting to investigate the narrow feature transport dynamics, and validating non-linear turbulence simulations to pinpoint their weaknesses and strengths, has been at least partially fulfilled.

A short summary of the observed dynamics and some concluding remarks now follow.

The C-Mod MLP profiles have two decay lengths, i.e., steep plasma profiles just outside the LCFS followed by a flatter gradient starting about 5 mm into the SOL (see Table III.). The GBS simulations exhibit similar steep gradients, but the narrow feature strength is underestimated with respect to the MLP data. The position of the narrow feature correlates with a layer of radially sheared $\mathbf{E} \times \mathbf{B}$ flows where the shear rate $\gamma_{\mathbf{E}\times\mathbf{B}}$ matches or exceeds the ballooning growth rate. The GBS simulations displayed sheared flows near the source location used as a "separatrix," where nonetheless the simulated $\gamma_{\mathbf{E}\times\mathbf{B}}$ frequency is not as strong as in C-Mod. Similar trends were recovered in simulations of the TCV IWL SOL dynamics, where GBS simulations were unable to reproduce the narrow feature strength observed in infrared thermography measurements of the inner-wall tiles.[54]

The large $\gamma_{\mathbf{E}\times\mathbf{B}}$ shear rate does not result in decreased correlation lengths or fluctuation amplitude. This effect was consistent across the MLP, GPI, and GBS data, which however did not show a definite trend (e.g., only the MLP data shows a decrease in relative fluctuation amplitude near the LCFS with respect to the far-SOL). The plasma filaments, as observed by the GPI, have a radial correlation length of the order of 10 mm, which decreases away from the LCFS. The mode ellipticity $L_{pol}/L_{rad} = k_{rad}/k_{pol} \approx 2$ does not vary significantly throughout the SOL and agrees with a recent analysis of GPI data, showing that $L_{rad} \sim L_{pol}$ in the plasma edge of L-mode, H-mode, and Ohmic NSTX plasmas.[55]

We remark that within the narrow feature, the plasma potential deviates substantially from its floating value ΛT_e, as shown in Fig. 2. This is indicative of currents flowing to or from the sheath into the plasma and affecting the dynamics, as has been observed previously in COMPASS and TCV.[4,5] In effect, a recent model has argued that the sheath currents can be used to estimate the turbulent transport.[45] In a simplified form, it is proposed that $\lambda_q \approx L_{rad}/(2\pi)(q_a R_0/\rho_s)^{1/4}$. Using the C-Mod data in Table I, together with the plasma potential correlation length ($L_{rad}(\phi) \approx$ 3 mm) from the GBS simulations, we obtain $\lambda_q \approx 4$–6 mm. This figure is comparable, although larger, than the C-Mod $\lambda_q \approx 3$ mm, but well below $\lambda_{q,main} \approx 15$–25 mm predicted by the mesoscale turbulent transport theory.[56]

To conclude, we remark that there is indication from MLP diagnostics, as well as from turbulence simulations, that the near-SOL profiles in C-MOD IWL plasmas are about 10 times steeper than the far-SOL profiles. The MLP and GBS simulations reveal the presence of significant sheared flows near the LCFS, although there is not enough evidence to suggest causality in the experimental data. Similarly, the GPI diagnostic shows an abrupt change the in propagation direction around the LCFS, although the exact location of this feature is uncertain and, in order to match the MLP data, was shifted 3 mm outward with respect to the equilibrium reconstruction position. The large $\gamma_{\mathbf{E}\times\mathbf{B}}$ does not translate into a negligible fluctuation amplitude. The transport mechanism described in Ref. 56 pointed towards sheath currents

and strongly sheared flows, however combined with large fluctuation amplitudes and unaffected correlation lengths. This picture is consistent with the C-Mod MLP and GPI data. Quantitative predictions and high fidelity simulations will need to capture equilibrium flows at the edge/SOL interface, at realistic plasma sizes, including neoclassical effects, and in the transport timescale of the confined plasma region.

ACKNOWLEDGMENTS

[1]M. Kocan, R. Pitts, G. Arnoux, I. Balboa, P. de Vries, R. Dejarnac, I. Furno, R. Goldston, Y. Gribov, J. Horacek, M. Komm, B. Labit, B. LaBombard, C. Lasnier, R. Mitteau, F. Nespoli, D. Pace, R. Panek, P. Stangeby, J. Terry, C. Tsui, and P. Vondracek, Nucl. Fusion **55**, 033019 (2015).

[2]J. Horacek, R. A. Pitts, J. Adamek, G. Arnoux, J.-G. Bak, S. Brezinsek, M. Dimitrova, R. J. Goldston, J. P. Gunn, J. Havlicek, S.-H. Hong, F. Janky, B. LaBombard, S. Marsen, G. Maddaluno, L. Nie, V. Pericoli, T. Popov, R. Panek, D. Rudakov, J. Seidl, D. S. Seo, M. Shimada, C. Silva, P. C. Stangeby, B. Viola, P. Vondracek, H. Wang, G. S. Xu, and Y. Xu, and JET Contributors, Plasma Phys. Controlled Fusion **58**, 074005 (2016).

[3]G. Arnoux, T. Farley, C. Silva, S. Devaux, M. Firdaouss, D. Frigione, R. Goldston, J. Gunn, J. Horacek, S. Jachmich, P. Lomas, S. Marsen, G. Matthews, R. Pitts, M. Stamp, P. Stangeby, and JET Contributors, Nucl. Fusion **53**, 073016 (2013).

[4]F. Nespoli, B. Labit, I. Furno, G. Canal, and A. Fasoli, J. Nucl. Mater. **463**, 393 (2014).

[5]R. Dejarnac, P. Stangeby, R. Goldston, E. Gauthier, J. Horacek, M. Hron, M. Kocan, M. Komm, R. Panek, R. Pitts, and P. Vondracek, in *Proceedings of the 21st International Conference on Plasma-Surface Interactions in Controlled Fusion Devices Kanazawa, Japan May 26–30*, 2014, [J. Nucl. Mater. **463**, 381 (2015)].

[6]P. Stangeby, C. Tsui, C. Lasnier, J. Boedo, J. Elder, M. Kocan, A. Leonard, A. McLean, R. Pitts, and D. Rudakov, in *Proceedings of the 21st International Conference on Plasma-Surface Interactions in Controlled Fusion Devices Kanazawa*, Japan May 26–30, 2014, [J. Nucl. Mater. **463**, 389 (2015)].

[7]E. Marmar, S. Baek, H. Barnard, P. Bonoli, D. Brunner, J. Candy, J. Canik, R. Churchill, I. Cziegler, G. Dekow, L. Delgado-Aparicio, A. Diallo, E. Edlund, P. Ennever, I. Faust, C. Fiore, C. Gao, T. Golfinopoulos, M. Greenwald, Z. Hartwig, C. Holland, A. Hubbard, J. Hughes, I. Hutchinson, J. Irby, B. LaBombard, Y. Lin, B. Lipschultz, A. Loarte, R. Mumgaard, R. Parker, M. Porkolab, M. Reinke, J. Rice, S.

Scott, S. Shiraiwa, P. Snyder, B. Sorbom, D. Terry, J. Terry, C. Theiler, R. Vieira, J. Walk, G. Wallace, A. White, D. Whyte, S. Wolfe, G. Wright, J. Wright, S. Wukitch, and P. Xu, Nucl. Fusion **55**, 104020 (2015).

[8]P. Ricci, F. D. Halpern, S. Jolliet, J. Loizu, A. Mosetto, A. Fasoli, I. Furno, and C. Theiler, Plasma Phys. Controlled Fusion **54**, 124047 (2012).

[9]F. Halpern, P. Ricci, S. Jolliet, J. Loizu, J. Morales, A. Mosetto, F. Musil, F. Riva, T. Tran, and C. Wersal, J. Comput. Phys. **315**, 388 (2016).

[10]F. D. Halpern, J. L. Terry, S. J. Zweben, B. LaBombard, M. Podesta, and P. Ricci, Plasma Phys. Controlled Fusion **57**, 054005 (2015).

[11]T. Eich, B. Sieglin, A. Scarabosio, W. Fundamenski, R. J. Goldston, A. Herrmann, and ASDEX Upgrade Team, Phys. Rev. Lett. **107**, 215001 (2011).

[12]M. A. Makowski, D. Elder, T. K. Gray, B. LaBombard, C. J. Lasnier, A. W. Leonard, R. Maingi, T. H. Osborne, P. C. Stangeby, J. L. Terry, and J. Watkins, Phys. Plasmas **19**, 056122 (2012).

[13]R. Goldston, J. Nucl. Mater. **463**, 397 (2015).

[14]B. LaBombard, R. L. Boivin, M. Greenwald, J. Hughes, B. Lipschultz, D. Mossessian, C. S. Pitcher, J. L. Terry, S. J. Zweben, and Alcator Group, Phys. Plasmas **8**, 2107 (2001).

[15]D. Rudakov, J. Boedo, R. Pitts, G. Jackson, C. Lasnier, A. Leonard, R. Moyer, P. Stangeby, G. Tynan, and J. Watkins, in *Proceedings of the 19th International Conference on Plasma-Surface Interactions in Controlled Fusion*, [J. Nucl. Mater. **415**, S387 (2011)].

[16]B. LaBombard, J. L. Terry, J. W. Hughes, D. Brunner, J. Payne, M. L. Reinke, I. Cziegler, R. Granetz, M. Greenwald, I. H. Hutchinson, J. Irby, Y. Lin, B. Lipschultz, Y. Ma, E. S. Marmar, W. L. Rowan, N. Tsujii, G. Wallace, D. G. Whyte, S. Wolfe, S. Wukitch, G. Wurden, and Alcator C-Mod Team, Phys. Plasmas **18**, 056104 (2011).

[17]V. Naulin and A. H. Nielsen, SIAM J. Sci. Comput. **25**, 104 (2003).

[18]D. A. Russell, J. R. Myra, D. A. D'Ippolito, T. L. Munsat, Y. Sechrest, R. J. Maqueda, D. P. Stotler, S. J. Zweben, and NSTX Team, Phys. Plasmas **18**, 022306 (2011).

[19]O. E. Garcia, V. Naulin, A. H. Nielsen, and J. J. Rasmussen, Phys. Rev. Lett. **92**, 165003 (2004).

[20]J. Horacek, "Measurement of edge electrostatic turbulence in the TCV tokamak plasma boundary," Ph.D. thesis No. 3524 (École Polytechnique Fédérale de Lausanne, Lausanne, 2006).

[21]J. R. Myra, D. A. Russell, D. A. DÍppolito, J.-W. Ahn, R. Maingi, R. J. Maqueda, D. P. Lundberg, D. P. Stotler, S. J. Zweben, J. Boedo, M. Umansky, and NSTX Team, Phys. Plasmas **18**, 012305 (2011).

[22]J. Myra, W. Davis, D. D'Ippolito, B. LaBombard, D. Russell, J. Terry, and S. Zweben, Nucl. Fusion **53**, 073013 (2013).

[23]S. J. Zweben, B. D. Scott, J. L. Terry, B. LaBombard, J. W. Hughes, and D. P. Stotler, Phys. Plasmas **16**, 082505 (2009).

[24]T. T. Ribeiro and B. Scott, Plasma Phys. Controlled Fusion **50**, 055007 (2008).

[25]N. R. Walkden, B. D. Dudson, and G. Fishpool, Plasma Phys. Controlled Fusion **55**, 105005 (2013).

[26]F. Militello, N. R. Walkden, T. Farley, W. A. Gracias, J. Olsen, F. Riva, L. Easy, N. Fedorczak, I. Lupelli, J. Madsen, A. H. Nielsen, P. Ricci, P. Tamain, and J. Young, Plasma Phys. Controlled Fusion **58**, 105002 (2016).

[27]C. Chang, S. Ku, A. Loarte, V. Parail, F. Koechl, M. Romanelli, R. Maingi, J.-W. Ahn, T. Gray, J. Hughes, B. LaBombard, T. Leonard, M. Makowski, and J. Terry, "Gyrokinetic projection of the divertor heat-flux width from present tokamaks to ITER," Nucl. Fusion (submitted); e-print at arXiv:1701.05507 .

[28]N. Smick and B. LaBombard, Rev. Sci. Instrum. **80**, 023502 (2009).

[29]B. LaBombard, T. Golfinopoulos, J. L. Terry, D. Brunner, E. Davis, M. Greenwald, J. W. Hughes, and Alcator C-Mod Team, Phys. Plasmas **21**, 056108 (2014).

[30]J. Horacek, P. Vondracek, R. Panek, R. Dejarnac, M. Komm, R. Pitts, M. Kocan, R. Goldston, P. Stangeby, E. Gauthier, P. Hacek, J. Havlicek, M. Hron, M. Imrisek, F. Janky, and J. Seidl, J. Nucl. Mater. **463**, 385 (2014).

[31]I. Cziegler, J. L. Terry, J. W. Hughes, and B. LaBombard, Phys. Plasmas **17**, 056120 (2010).

[32]S. J. Zweben, J. L. Terry, D. P. Stotler, and R. J. Maqueda, Rev. Sci. Instrum. **88**, 041101 (2017).

[33]F. Riva, P. Ricci, F. D. Halpern, S. Jolliet, J. Loizu, and A. Mosetto, Phys. Plasmas **21**, 062301 (2014).

[34]P. Ricci, F. Riva, C. Theiler, A. F. Fasoli, I. Furno, F. D. Halpern, and J. Loizu, Phys. Plasmas **22**, 055704 (2015).

[35]A. Zeiler, J. F. Drake, and B. Rogers, Phys. Plasmas **4**, 2134 (1997).

[36]C. Wersal and P. Ricci, Nucl. Fusion **55**, 123014 (2015).

[37]S. I. Braginskii, "Transport processes in a plasma," in *Reviews of Plasma Physics*, edited by M. A. Leontovich (Consultants Bureau, New York, 1965), Vol. 1, p. 205.

[38]B. Dudson, M. Umansky, X. Xu, P. Snyder, and H. Wilson, Comput. Phys. Commun. **180**, 1467 (2009).

[39]P. Tamain, H. Bufferand, G. Ciraolo, C. Colin, D. Galassi, P. Ghendrih, F. Schwander, and E. Serre, J. Comput. Phys. **321**, 606 (2016).

[40]J. Morales, B. Frei, F. Halpern, F. Musil, P. Paruta, P. Ricci, F. Riva, M. Siffert, and C. Wersal, in 43rd EPS Conference on Plasma Physics, *P4.030* (Leuven, Belgium, 2016).

[41]A. Mosetto, F. D. Halpern, S. Jolliet, J. Loizu, and P. Ricci, Phys. Plasmas **22**, 012308 (2015).

[42]P. Manz, G. Birkenmeier, D. Carralero, G. Fuchert, H. W. Müller, S. H. Müller, B. D. Scott, U. Stroth, T. T. Ribeiro, and E. Wolfrum, Plasma Phys. Controlled Fusion **57**, 014012 (2015).

[43]B. Zhu, M. Francisquez, and B. N. Rogers, Phys. Plasmas **24**, 055903 (2017).

[44]J. Loizu, P. Ricci, F. D. Halpern, and S. Jolliet, Phys. Plasmas **19**, 122307 (2012).

[45]F. Halpern and P. Ricci, Nucl. Fusion **57**, 034001 (2017).

[46]D. Stotler, J. Boedo, B. LeBlanc, R. Maqueda, and S. Zweben, J. Nucl. Mater. **363–365**, 686 (2007).

[47]R. Futtersack, C. Colin, P. Tamain, G. Ciraolo, P. Ghendrih, Y. Marandet, F. Schwander, and E. Serre, Contrib. Plasma Phys. **56**, 575 (2016).

[48]A. Mosetto, F. D. Halpern, S. Jolliet, and P. Ricci, Phys. Plasmas **19**, 112103 (2012).

[49]C. K. Tsui, J. A. Boedo, F. D. Halpern, J. Loizu, F. Nespoli, J. Horacek, B. Labit, J. Morales, H. Reimerdes, P. Ricci, C. Theiler, B. Duval, S. Coda, I. Furno, and TCV Team, Phys. Plasmas **24**, 062508 (2017).

[50]C. Theiler, I. Furno, P. Ricci, A. Fasoli, B. Labit, S. H. Müller, and G. Plyushchev, Phys. Rev. Lett. **103**, 065001 (2009).

[51]S. I. Krasheninnikov, D. A. D'Ippolito, and J. R. Myra, J. Plasma Phys. **74**, 679 (2008).

[52]B. N. Rogers and W. Dorland, Phys. Plasmas **12**, 062511 (2005).

[53]D. A. Russell, J. R. Myra, D. A. D'Ippolito, B. LaBombard, J. W. Hughes, J. L. Terry, and S. J. Zweben, Phys. Plasmas **23**, 062305 (2016).

[54]F. Nespoli, I. Furno, F. Halpern, B. Labit, J. Loizu, P. Ricci, and F. Riva, "Non-linear simulations of the TCV scrape-off layer," Nucl. Mater. Energy (published online).

[55]J. R. Myra, D. A. Russell, and S. J. Zweben, Phys. Plasmas **23**, 112502 (2016).

[56]F. D. Halpern, J. Horacek, R. A. Pitts, and P. Ricci, Plasma Phys. Controlled Fusion **58**, 084003 (2016).